

HOT AND SUPERHOT PLASMAS ABOVE AN IMPULSIVE FLARE LOOP

SAKU TSUNETA,¹ SATOSHI MASUDA,² TAKEO KOSUGI,¹ AND JUN SATO¹

Received 1996 May 7; accepted 1996 October 23

ABSTRACT

We report the discovery of a high-temperature source above the soft X-ray loop of the impulsive limb flare on 1992 January 13 with the *Yohkoh* Soft X-ray Telescope (SXT). The hot source coincides in position with the loop-top impulsive hard X-ray source and continues to sit above the soft X-ray flare loop throughout the flare. The single high-temperature source in the initial phase evolves to the two high-temperature (15–20 MK) ridge structures in the peak and decay phases, and the compact hard X-ray source appears to be located in between the high-temperature ridges. We assume that the loop-top hard X-ray source is of thermal origin (superhot source). The loop-top hard X-ray source has an effective temperature of 100–150 MK and a total emission measure of $\sim 10^{-4}$ of the hot source. The geometrical relationship between the superhot and the hot sources indicates that (1) the hot source is heated by the slow shocks associated with magnetic reconnection and that (2) the superhot source is heated with the fast bow shock owing to the collision of the supersonic downward outflow with the reconnected flux tube. The small emission measure of the superhot source indicates a narrow outflow jet in between the slow shocks. These observations suggest that there is no essential difference between the compact-loop (impulsive) and long-duration event (LDE) flares. The time coincidence of the loop-top hard X-ray source with the footpoint sources indicates that nonthermal electron acceleration is causally related to the formation of the fast shock rather than the slow shocks.

Subject headings: MHD — Sun: flares — Sun: X-rays, gamma rays

1. INTRODUCTION

Recent observations with *Yohkoh* X-ray telescopes (Ogawara et al. 1991 and references therein) suggest that magnetic reconnection (see, e.g., Petschek 1964; Priest & Forbes 1986) is responsible for various transient heatings in the solar corona. In particular, Tsuneta et al. (1992) and Tsuneta (1996a) concluded from the detailed analysis of the 1992 February 21 long-duration event (LDE) that (1) magnetic reconnection occurs at a neutral sheet or at an X-type neutral point above the reconnected loop, (2) the standing slow shocks attached to the diffusion point (X-point) play an important role in converting the magnetic energy to the plasma thermal and kinetic energies, and (3) the Petschek reconnection configuration (X-point plus slow shock structures) fits well with the *Yohkoh* soft X-ray data for the flare (see also Forbes & Acton 1996). Other LDE flares observed with *Yohkoh* have observational features quite similar to those of the 1992 February 21 flare (see also MacCombie & Rust 1979). Therefore, it is likely that magnetic reconnection is responsible for the LDE-type flares, which has been predicted by several authors (Petschek 1964; Carmichael 1964; Sturrock 1966; Hirayama 1974; Kopp & Pneuman 1976; Cargill & Priest 1983; Ugai 1987; Forbes & Malherbe 1991; Yokoyama 1995; Magara et al. 1996), although the mechanism for the formation of the neutral sheet (X-point), probably as a result of active region eruption (Tsuneta 1993; Shibata et al. 1995a), has not yet been understood. Note that these observations do not rule out other types of reconnection configurations as flare mechanisms, such as loop-loop reconnection (Yoshida & Tsuneta 1996; Shimizu et al. 1992, 1994) and emerging flux reconnection (Shibata, Yokoyama, & Shimojo 1995b; Yokoyama & Shibata 1996; Shimojo et al. 1996).

Solar flares have been classified into two types: two ribbon (and LDE) flares and simple loop flares as revealed by *Skylab* observations (see, e.g., Sturrock 1980). Indeed, *Yohkoh* has observed both giant cusp-shaped (arcade) flares and simple compact-loop flares, and the two types of flares appear to be different. The time variability of compact flares is higher (impulsive) than LDE-type flares (gradual), and impulsive flares tend to have more of a nonthermal nature than LDE flares. (There is also a gradual transition from the impulsive phase to the gradual phase in an impulsive flare.)

These apparent differences between LDE and compact flares imply different physical mechanisms involved in the flare energy release. There are two *Yohkoh* observations that shed light on this observational discrepancy between LDE-type and impulsive-type flares:

1. Masuda et al. (1994) discovered impulsive hard X-ray sources located above the loop top with relatively hard spectra (hereafter referred to as the loop-top hard X-ray source, following Masuda et al. 1994) in addition to the usual double footpoint sources for several impulsive limb flares and suggested that magnetic reconnection takes place around or above the loop-top hard X-ray source.

2. Tsuneta (1993) and Shibata et al. (1995a) found rising (plasmoid) structures for flares with the loop-top hard X-ray source and inferred that magnetic reconnection occurs at the X-point, created as a result of the global eruption of active region magnetic fields. These observations may allow us to understand solar flares in general from a unified point of view (Shibata et al. 1995a).

However, no direct observation to support magnetic reconnection for impulsive flares has been reported so far. Therefore, it is important to clarify observationally the structure of the loop-top region with both the Hard X-ray Telescope (HXT) and the Soft X-ray Telescope (SXT) aboard *Yohkoh*. This paper further examines the data for the well-observed flare reported by Masuda et al. (1994,

¹ National Astronomical Observatory, Mitaka, Tokyo 181, Japan.

² STE Laboratory, Nagoya University, Toyokawa, Aichi 442, Japan.

1995) and Shibata et al. (1995a) and reports the discovery of the high-temperature (15–20 MK) source coincident in position with the impulsive loop-top hard X-ray source. We then argue that there is no essential difference between the compact-loop (impulsive) and long-duration (LDE) flares and that both types of flares are explained with magnetic reconnection.

2. LOOP-TOP HOT SOURCE

2.1. Temperature Map

Figure 1 shows the hard X-ray time profile of the 1992 January 13 flare. The flare was a GOES M2.0 flare and has a single spike with a FWHM duration of about 1 minute above 30 keV. The time profiles of the loop-top hard X-ray source and the footpoint sources are also shown as triangles and plus signs, respectively, in Figure 1 (Masuda et al. 1994). Figure 2 (Plate 20) shows the temperature and emission measure maps of the early phase obtained with SXT. A compact high-temperature source (hereafter referred to as the hot source) is clearly seen above the top of the flare loop. The hot source is located where the X-ray intensity is only a few percent to 10% of the peak X-ray intensity of the flare loop.

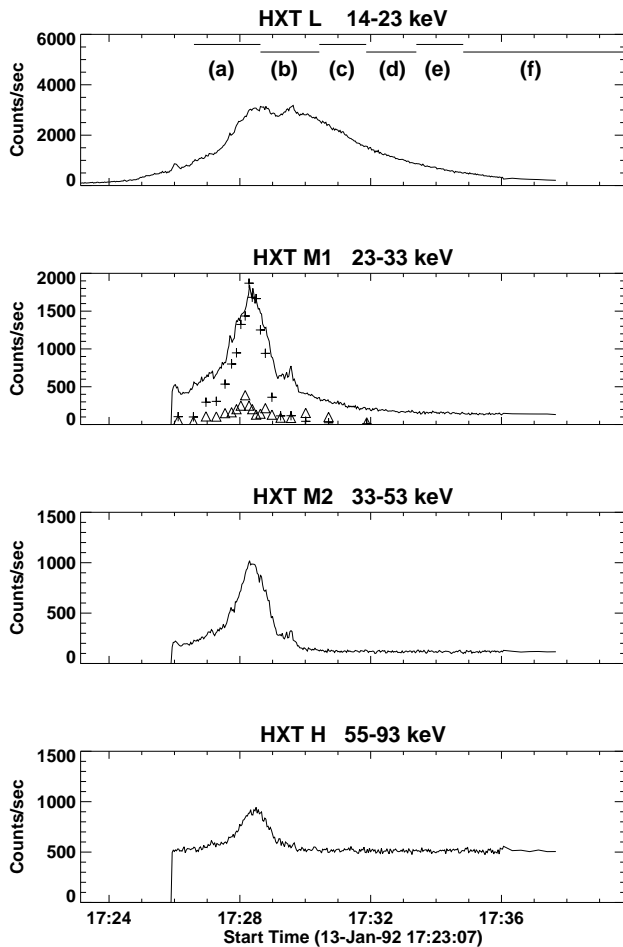


FIG. 1.—Hard X-ray time profile of the 1992 January 13 flare taken with HXT. Higher energy band data are not available before \sim UT 17:26 when the flare-mode recording was triggered. The time profiles of the double footpoint sources (*plus signs*) and the loop-top source (*triangles*) in HXT M1 channel (23–33 keV) are also shown (arbitrary scale, taken from Masuda et al. 1994). SXT exposure times for the temperature maps of Figs. 3a–3f are shown in the top panel.

The temperature maps are obtained from the ratio of two images taken with two different filters. Isothermality within a single SXT pixel is assumed in the temperature analysis. The thick aluminum and beryllium filters are used for the temperature analysis throughout this paper. The uncertainty in the derived temperatures is discussed in §§ A1, A2, and A3 of the Appendix to this paper and is generally less than 10% in the flare loop and the hot source. Aligned multiple frames (six–nine frames, about 2 minutes in the early phase) are summed to improve the photon statistics. Note that the time integration over 2 minutes in the impulsive phase does not produce any systematic artifact in the derived temperature maps for the following reasons:

1. The images with the two filters have been taken in an interleaved manner. This arrangement makes the temperature maps less susceptible to the time variations.
2. The time profiles of the HXT L channel (14–23 keV) and the SXT light curve are gradual and do not change during the summation period.
3. The time sequence of the derived temperature maps shows a gradual change in the temperature structure (Fig. 3). A 3×3 smoothing of the SXT full-resolution pixel ($2''.46$) is also done (before the temperature analysis) to improve the photon statistics of the dark region above the flare loop.

Figure 2 also shows the contours of the hard X-ray maps from 14 to 53 keV overlaid on the temperature and density maps. The hard X-ray maps and their alignment with respect to the soft X-ray images are the same as those used in Masuda et al. (1994). The alignment error is less than a single SXT pixel ($2''.46$). The usual hard X-ray sources are located at the footpoints of the bright flare loop; the loop-top hard X-ray source essentially coincides in position with the hot source. The FWHM size of the hot source is larger than that of the hard X-ray source. Note that the loop-top hard X-ray source (33–53 keV) is not located at the position of the peak temperature of the hot source: The loop-top hard X-ray source is located to the north of the temperature peak at 17:27 UT (Figs. 2a and 3a) and is located in between the two temperature peaks at 17:28 UT (Figs. 2b and 3b). The temperature where the loop-top hard X-ray source is located is 1–3 MK lower than the peak temperatures. A slight increase in the temperature around the loop-top hard X-ray source can be noticed in Figure 1 of Masuda et al. (1994). The present analysis clearly shows a significant hot source above the loop top, owing to the improved photon statistics of the summed images.

Figure 3 (Plate 21) shows the temperature and emission measure maps from the start of the flare through the decay phase of the flare. The hot source stays above the flare loop even after the disappearance of the loop-top hard X-ray source and sits above the loop top throughout the flare. The peak temperature is about 20 MK in the early phase. The hot source has a longer horizontal length along the flare loop. Table 1 summarizes the temperature, the total emission measure, and other parameters of the hot source, assuming the line-of-sight thickness to be 10^4 km. The single hot source located above the flare loop (Fig. 3a) evolves to the structure with two temperature peaks (Figs. 3b and 3c). The separation of the two temperature humps increases with time (Figs. 3d and 3e). A triangular cusplike temperature structure (10–15 MK) is seen above the hot source in the decay phase (Figs. 3d and 3e). Figure 3 also shows the contours of the emission measure (20% and 1%

TABLE 1
LOOP-TOP HOT AND SUPERHOT COMPONENTS

Parameter	Superhot Source	Hot Source
Temperature (MK)	133 ^a	20
Total emission measure (cm ⁻³)	10 ^{44a}	2 × 10 ⁴⁸
Mean emission measure (cm ⁻⁵)	3 × 10 ²⁶	4 × 10 ²⁹
Density (cm ⁻³)	3 × 10 ⁹	2 × 10 ¹⁰
Pressure (dyn cm ⁻²)	112	112
Volume filling factor	2 × 10 ⁻³	1
Thermal energy content (ergs)	1.7 × 10 ²⁷	8.4 × 10 ²⁹

^a Masuda et al. 1994.

of the peak emission measure in each map). The 1% contours show that the emission measure (plasma density) around the region between the two temperature humps is somewhat enhanced (Figs. 3d and 3e).

The loop-top hard X-ray source appears at the very beginning of the impulsive phase (at around 17:26 UT) and disappears at around 17:29 UT in M2 channel (33–53 keV). A separate hard X-ray source appears in the L (14–23 keV) and M1 (23–33 keV) channels in the gradual phase (Masuda 1994): this source has a looplike structure and coincides in position and shape with the soft X-ray loop. This hard X-ray source is evidently of thermal origin and is the hard X-ray counterpart of the soft X-ray loop. This gradual hard X-ray source is different from the impulsive hard X-ray source located above the soft X-ray loop. The hot source continues to be located above the coincident soft and hard X-ray loop structures throughout in the decay phase.

2.2. Time Evolution of Flare Loop and Hot Source

Figure 4 shows the time profiles of the physical parameters at the point where the plasma pressure is the highest in the maps of Figures 3a–3f. This position corresponds to the bright top of the flare loop. (The hot source is located above this pressure peak.) The temperature is around 10–12 MK, which is much lower than that of the hot source. The emission measure, pressure, and density increase during the flare-mode observation. The peak density reaches $1.2 \times 10^{11} \text{ cm}^{-3}$, and the peak pressure reaches 320 dyn cm^{-2} . (The line-of-sight thickness is assumed to be 10^4 km . Even if the line-of-sight thickness is 1 order of magnitude smaller or larger than the assumed 10^4 km , the derived plasma density and pressure differ only by a factor of 3.2.) The height of the flare loop increases from 8600 km above the photosphere to 10,300 km over 8 minutes. The average speed of the rise is 3.5 km s^{-1} . The hot source is always located above the flare loop.

The time evolution of the hot source, on the other hand, is quite different. The dashed lines of Figure 4 show the evolution of the hot source. The temperature of the hot source is between 15 and 20 MK and peaks at the impulsive phase. The emission measure, plasma density, and plasma pressure are almost constant, whereas those of the flare loop located below significantly increase. This indicates that the hot source is not affected by chromospheric evaporation.

We point out that it is unlikely that the hot source is due to the dissipation of the nonthermal electrons for the following reasons. (Here, we assume that the loop-top hard X-ray source is entirely due to nonthermal electrons.)

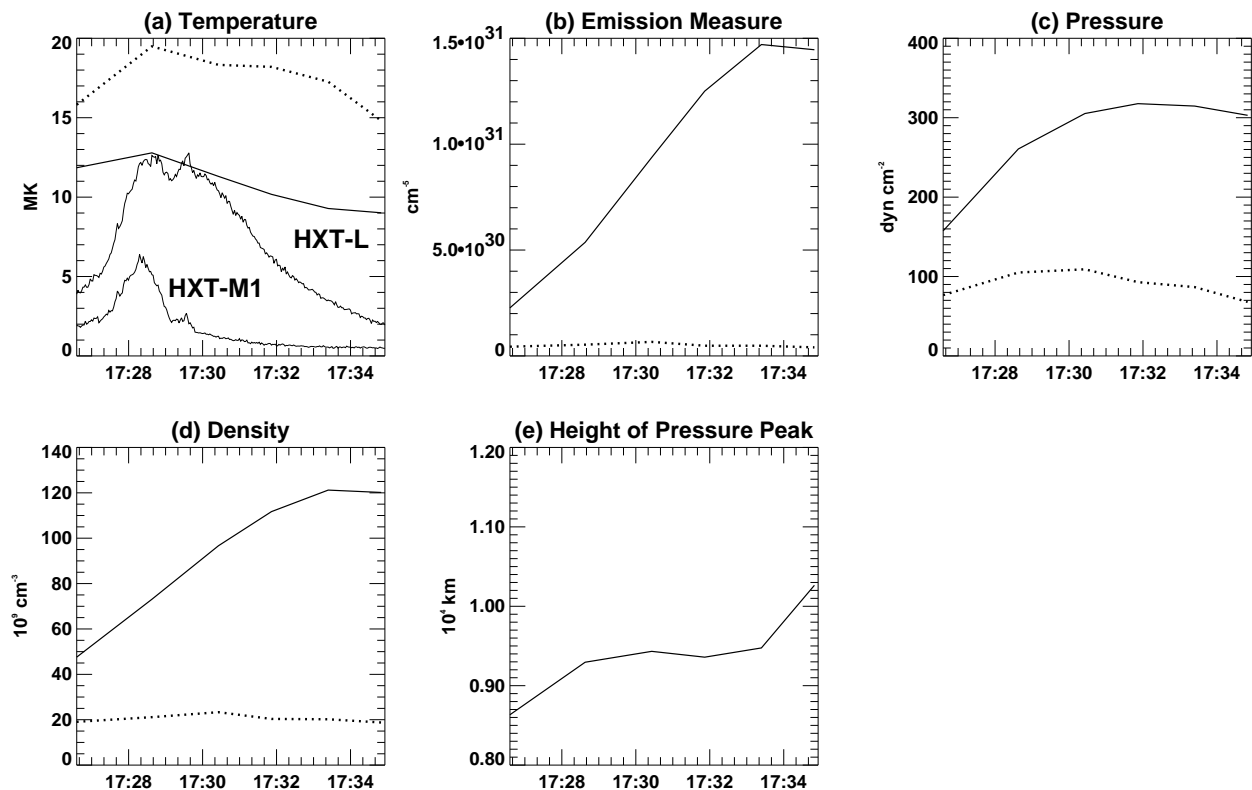


FIG. 4.—Thick lines show the time profiles of (a) temperature, (b) emission measure, (c) plasma pressure, (d) plasma density, and (e) height of the point where the pressure is the highest (top of the soft X-ray loop) in each map in Figs. 3a–3f. The height of the peak pressure increases as a function of time. The time profiles of the HXT L (14–23 keV) and M1 (23–33 keV) channels are also shown in (a). Dotted lines show the same parameters for the hot source above the flare loop. Average values of the hot source within the area with temperatures higher than 85% of the peak temperature (core of the hot source) are plotted as a function of time.

1. The hot source exists well after the disappearance of the loop-top hard X-ray source. The timescale of the dominant conductive cooling is about 18 s (§ 2.5), which is much shorter than the decay timescale of the hot component. Therefore, we need a continuous heat input to maintain the hot source after the fade-out of the loop-top hard X-ray source.

2. The shape of the hot source is quite different from that of the hard X-ray source. The hot source has two humps in temperature, and the compact hard X-ray source is located in between. We thus conclude that the hot source is directly heated by magnetic reconnection as will be discussed in the next subsection.

2.3. Magnetic Reconnection

The observations reported here are quite similar to those of an LDE flare of 1992 February 21 (Tsuneta et al. 1992; Tsuneta 1996a; Forbes & Acton 1996):

1. The hot source is located above the flare loop.
2. The hot source has two humps in temperature, and the region in between them has a lower temperature (cool channel).
3. The cool region in between the hot humps above the flare loop has a higher plasma density. (The nature of the cool channel will be discussed in the next subsection.)
4. The height of the reconnected loops increases with average speed of 3.5 km s^{-1} .

All these observed features indicate that magnetic reconnection is responsible for the heating of the hot source and that the bright soft X-ray loop is the resulting reconnected flux tube filled with the outflow plasma from the reconnection site and the plasma evaporated from the chromosphere. The constant emission measure of the hot component indicates that reconnection continues throughout the flare in a steady manner and that the reconnection site (diffusion region plus slow shock structure) is not affected by the chromospheric evaporation.

2.4. Observed Structure of the Reconnection Site

As discussed in the previous subsection, the fact that both the hot and the loop-top hard X-ray source are clearly located above the soft X-ray loop strongly suggests magnetic reconnection. In this subsection, we examine the temperature and density structure of the hot source in more detail. Figure 6 shows the temperature, density, and pressure distributions along the lines shown in Figure 5 (Plate 22), (1)–(6). The vertical lines (1)–(3) and the horizontal lines (4)–(6) go through the loop-top region including the hot source.

The plasma density and pressure (Fig. 6) increase with decreasing height (toward smaller pixel number in Fig. 6). The peak in the vertical density profiles corresponds to the loop-top region where the plasma density is the highest, probably owing to the reconnection outflow. The vertical temperature profile has a peak near the vertical pixel number ~ 18 . If this is the true temperature distribution (see Appendix, § A3), the sharp peak indicates that the heat source is concentrated at the peak position: The reconnection point and the slow shock structure must be located around the temperature peak.

Note, however, that the temperatures derived with broadband filters are line-of-sight-averaged temperatures. The line-of-sight nonflaring emission measure, presumably with lower temperature, decreases the derived temperatures

from the true temperature of the flare plasma, as the height increases and the emission measure of the flare plasma decreases with respect to that of the active region. Section A3 in the Appendix shows that it is possible that the hot source extends higher in the corona, though this is not clearly seen in the derived temperature maps owing to the more dominant contribution of the active region corona at higher altitudes.

The horizontal profiles (Fig. 6, [4]–[6]) show broader temperature peaks. Two temperature humps are seen along the horizontal line (5). The two peaks correspond to the slow shock location, where the heat is preferentially injected. The broad temperature peak is associated with the increase of the plasma density and pressure. This may correspond to the slight enhancement of the emission measure above the temperature peak (upward tongue-shaped structure seen in Fig. 3e) or may simply reflect the extension of the loop structure.

These observations are indeed consistent with the reconnection picture proposed for LDE flares (Fig. 6 of Tsuneta 1996a). Here, we discuss how the cool region in between the hot humps is formed. If the hot humps and the cool region in between are connected by magnetic fields, we should not have had such a cool region due to high thermal conduction. (Radiation loss is negligibly small.) Therefore, the hot source and the cool region in between must be insulated by magnetic fields. The field lines that go through the outer boundaries of the two hot ridges are magnetic separatrix lines and reach the X-point, whereas the field lines that go through the cool region approach the soft X-ray loop with the reconnection outflow jet: The field lines around the cool region are cusp shaped. Therefore, we reach a magnetic structure that is the same as the one established for LDE flares (Tsuneta 1996a; Forbes & Acton 1996).

The outflow jet heated by the slow shocks is thus cooled by heat conduction along the reconnected field lines, as they move downward with the reconnection jet. Thus, the temperature of the outflow plasma just below the X-point gradually decreases toward the flare loop. Indeed, this is seen in the vertical profiles of Figure 6. If the location of the primary heating is much higher, as in the 1992 February 21 flare, conductive cooling would produce a more distinct cool channel. This indicates that the distance between the reconnected flux tubes (soft X-ray loops) and the X-point in this flare is not as large as that of the 1992 February 21 flare.

2.5. Quantitative Analysis of the Slow Shock Structure

In this section, we try to determine the global slow shock structure from SXT observations and examine whether the hot source is quasi-steadily heated by the slow shocks. The equations used in this paper and Tsuneta (1996a) are derived in Tsuneta (1996b). CGS gauss units are used throughout the papers except where noted. We assume that the shock is switch off (see, e.g., Priest 1982, p. 189) and that the normal component of the magnetic field in the upstream side is zero. This is a good assumption for shocks associated with the Petschek-type magnetic reconnection with a small angle between the slow shocks. From the pressure balance across the shock, we obtain

$$p_h = p_u + \frac{B_u^2}{8\pi}, \quad (1)$$

where p_h and p_u are the observed downstream (hot source) and upstream plasma pressures. The quantity B_u is the mag-

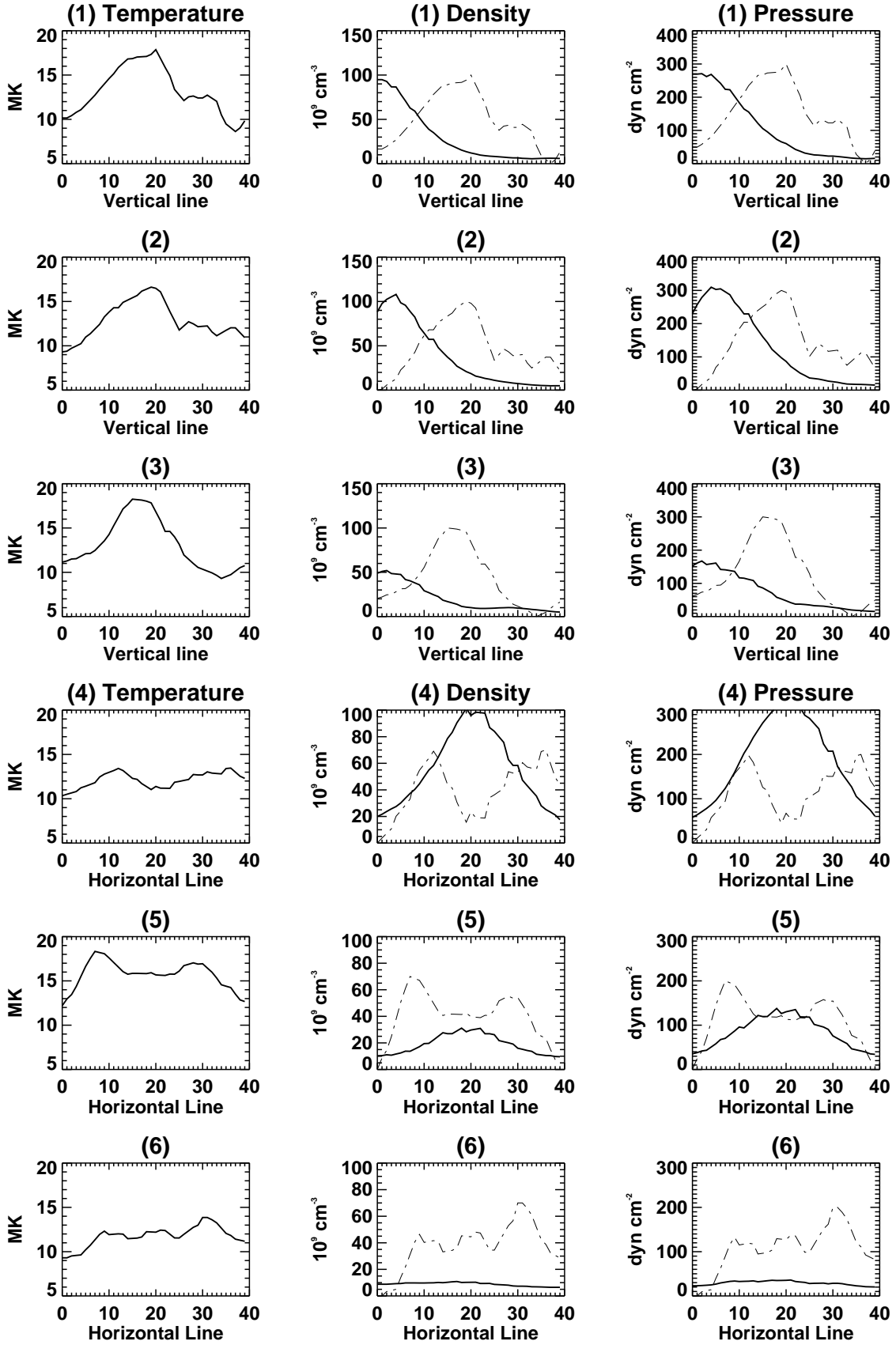


FIG. 6.—Temperature, density, and pressure distributions along the lines shown in Fig. 5: (1)–(3), vertical lines (smaller number in the horizontal axis for lower height); (4)–(6), horizontal lines (smaller number in the horizontal axis for north side). The dot-dashed lines in the density and pressure profiles are the temperature profiles. Horizontal line has unit of $1/2$ (889 km); half of SXT full resolution pixel. The image data taken between 17:31:51 and 17:33:23 UT is summed for these plots. Line-of-sight thickness of 10^4 km is assumed for density and pressure distributions.

netic field strength of the upstream plasma, which is estimated to be about 52 G for $p_h = 120 \text{ dyn cm}^{-2}$ and $p_u = 10 \text{ dyn cm}^{-2}$ (Fig. 6 [5]). [If the shock angle is narrow, the density jump associated with the slow shocks will not be clearly seen in the SXT images. This may underestimate the plasma-pressure difference ($p_h - p_u$), which will result in a lower estimate of the magnetic field strength of the upstream side.] The plasma β of the upstream plasma is $\beta = 8\pi p_u/B_u^2 \sim 0.09$. (The plasma β is much larger than 1 in the downstream region owing to the assumption of the switch off shock and the small angle of the slow shocks.) The field strength for this flare is considerably larger than that of the 1992 February 21 flare (20–30 G). This may be consistent with the lower height of the X-point of the present flare. The outflow velocity V_h is the Alfvén velocity of the upstream plasma and is about 1144 km s^{-1} for $B_u \sim 52 \text{ G}$, $n_u \sim 10^{10} \text{ cm}^{-3}$. The sound speed of the downflow is about $742 \text{ (20 MK)–642 (15 MK) km s}^{-1}$, and the sound Mach number is 1.5–1.8.

We next examine the energetics of the reconnection site. We assume that the energy produced in the reconnection site goes into the slow shock heating as well as energy of the bulk flow. This assumption is good for the Petschek reconnection model, where the slow shock angle is small and the downstream plasma β is high. The heat produced by the shock can be estimated from conduction loss,

$$E_H \sim s_h \kappa_0 T_h^{7/2}/l_h, \quad (2)$$

where $\kappa_0 T_h^{5/2}$ is the Spitzer thermal conductivity ($\kappa_0 = 10^{-6} [\text{ergs s}^{-1} \text{ cm}^{-1} \text{ K}^{-3.5}]$), l_h is the scale length, and s_h is the cross-sectional area of the hot source. The observed temperature gradient is about $15 \text{ MK}/(l_h \sim 2 \times 10^4 \text{ km})$ along the curved reconnected field lines. The conduction flux is about $5.3 \times 10^{27} \text{ ergs s}^{-1}$ for $s_h = (9 \times 10^3 \text{ km})^2$, which is approximately the square of the vertical FWHM size of the hot source. The kinetic energy of the outflow is estimated to be

$$E_{\text{flow}} = \frac{m_p}{2} (n_h s_d V_h) V_h^2 + \frac{5}{2} p_h s_d V_h, \quad (3)$$

where s_d is the cross-sectional area of the outflow, p_h is the plasma pressure of the outflow, and m_p is the proton rest mass. The flow energy is $1.1 \times 10^{27} \text{ ergs s}^{-1} + 1.3 \times 10^{27} \text{ ergs s}^{-1} = 2.4 \times 10^{27} \text{ ergs s}^{-1}$ for $p_h \sim 50 \text{ dyn cm}^{-2}$ and $n_h \sim 10^{10} \text{ cm}^{-3}$. Here, we assume that the horizontal width of the outflow jet is the same as the observed horizontal FWHM width of the loop-top hard X-ray source in 33–53 keV channel (Fig. 2); $s_d = (3 \times 10^3 \text{ km})^2$. The total energy dissipation due to magnetic reconnection is $E_B = E_H + E_{\text{flow}} \sim (2.4 + 5.3 = 7.7) \times 10^{27} \text{ ergs s}^{-1}$.

This energy dissipation rate has to balance with the inflow magnetic energy:

$$E_B = \frac{B_u^2}{4\pi} s_u V_u, \quad (4)$$

where s_u is the cross-sectional area of the reconnection site in the upstream side. In order to supply the energy $E_B \sim 7.7 \times 10^{27} \text{ ergs s}^{-1}$, the inflow velocity is 71 km s^{-1} for $B_u \sim 52 \text{ G}$, and the area of the inflow region $s_u \sim 5 \times 10^4 \text{ km}$ (vertical length) $\times 10^4 \text{ km}$ (line-of-sight length). The Alfvén Mach number of the inflow is $71 \text{ km s}^{-1}/1144 \text{ km s}^{-1} = 0.06$. Table 2 summarizes these parameters. The

TABLE 2
PHYSICAL PARAMETERS OF RECONNECTION REGION

Parameter	Upstream	Downstream
Temperature (MK)	3–5	~20
Density (cm^{-3}).....	10^{10}	$\sim 2 \times 10^{10}$
Pressure (dyn cm^{-2}).....	10	120
Magnetic field (G)	52	...
Plasma β	0.09	≥ 1
Flow velocity (km s^{-1}).....	41–71	1144
Sound Mach number.....	0.1–0.2	1.5–1.8
Alfvén Mach number.....	0.04–0.06	...
Alfvén speed (km s^{-1}).....	1144	...
Sound speed (km s^{-1}).....	371	642–742
Input energy (ergs s^{-1}).....	7.7×10^{27}	...
Output energy (ergs s^{-1}).....	...	7.7×10^{27}

inflow speed can also be obtained from mass conservation:

$$V_u = V_h \frac{s_d n_h}{s_u n_u}, \quad (5)$$

where s_d and s_u are the cross-sectional areas of the inflow and outflow. We obtain the inflow velocity of 41 km s^{-1} for $n_h/n_u \sim 2$ and the above parameters. Thus, the two independent estimates give an inflow speed range of $41\text{--}71 \text{ km s}^{-1}$. The duration of the flare in the HXT L channel (14–23 keV) is about 4 minutes (FWHM width). Thus, the field lines in the upstream region with half-lengths of $41\text{--}71 \text{ km s}^{-1} \times 4 \text{ minutes} \sim 10^4\text{--}1.7 \times 10^4 \text{ km}$ reconnect during the flare. This size is consistent with the size of the flare loop. (The size can be smaller, if the field strength in the upstream side is larger.)

Finally, we examine whether the cool region can be formed by the conductive cooling along the reconnected field lines. The radiative cooling time of the hot source is expressed as

$$t_{\text{rad}} = \frac{3n_h k T_h}{\Lambda(T_h) n_h^2}, \quad (6)$$

where k is the Boltzmann constant and $\Lambda(T_h)$ is the radiative loss function. Since the density $n_h \sim 2 \times 10^{10} \text{ cm}^{-3}$, the temperature $T_h \sim 20 \text{ MK}$, and the radiative loss function $\Lambda(T_h) = 6 \times 10^{-20} T_h^{-0.5}$, the radiative cooling time t_{rad} is $3 \times 10^4 \text{ s}$ (8.7 hr). Thus, radiative cooling is too slow to cool the outflow, and the cool region in between the hot humps is due to conductive cooling along the reconnected field lines as discussed in § 2.4. The conductive cooling time is given by

$$t_{\text{cond}} = \frac{3n_h k T_h l_h}{\kappa_0 T_h^{5/2} (T_h/l_h)}, \quad (7)$$

where $\kappa_0 T_h^{5/2}$ is the Spitzer thermal conductivity ($\kappa_0 = 10^{-6} [\text{ergs s}^{-1} \text{ cm}^{-1} \text{ K}^{-3.5}]$), and l_h is the scale length of the hot source. The conduction timescale t_{cond} is 18 s for $l_h = 2 \times 10^4 \text{ km}$. If the X-point (diffusion point) is located $2 \times 10^4 \text{ km}$ above the hot source, as suggested by the triangular-shaped enhanced temperature distribution in Figures 3d and 3e, it will take about $2 \times 10^4 \text{ km}/1134 \text{ km s}^{-1} \sim 18 \text{ s}$ for the outflow jet to travel from the X-point to the hot source. This timescale is comparable to the conductive cooling timescale estimated above. This indicates that conductive cooling can form the observed cool region in between the high-temperature humps even for a low X-point location.

3. ORIGIN OF THE SUPERHOT SOURCE

3.1. Location of the Hard X-Ray Source in the Hot Source

It is important to know exactly where the hard X-ray source is located in the hot source and in the inferred overall magnetic structure of the reconnection site. In the vertical profile presented in § 2.4, the loop-top hard X-ray source is located near the temperature peak of the hot source; it is located where the pressure starts to increase in the vertical pressure profile. In the horizontal profile, the loop-top hard X-ray source is located in between the temperature humps. The temperature of the hot source where the hard X-ray source is located is slightly lower (Fig. 2*b*). Thus, the hard X-ray source is located in the cooling outflow jet in between the slow shocks. The outflow jet has a lower temperature with lower altitude from the reconnection point, owing to conductive cooling along the reconnected field lines (§ 2.5). The location of the hard X-ray source strongly supports the inference by Masuda et al. (1994) and Shibata et al. (1995a) that the loop-top hard X-ray source is heated by the fast shock in the supersonic outflow from the reconnection site.

3.2. Thermal versus Nonthermal?

3.2.1. Nonthermal Interpretation

In this section, we discuss whether the impulsive hard X-rays from the loop top are due to bremsstrahlung from nonthermal electrons or from thermal electrons. First of all, we assume that the loop-top hard X-ray source is due to bremsstrahlung from nonthermal electrons. Since there is no localized plasma density enhancement from SXT observations, it is not possible to explain the loop-top hard X-ray source by enhancement of the target (background) plasma density (e.g., with a uniform nonthermal electron distribution, thin-target concept). (We cannot rule out the possibility that the plasma that is too cool to be seen by SXT is located at the hard X-ray source. However, since there is no hard X-ray emission from the denser soft X-ray loop, it is difficult to explain the loop-top hard X-ray emission with thin-target emission.)

An alternative explanation is that nonthermal electrons are confined, and their energy is dissipated there (thick-target emission; Brown 1971). The thick-target energy deposited at the loop-top hard X-ray source amounts to $\geq 10^{27}$ ergs s^{-1} (Masuda 1994). The column density N of the target thermal plasma is $N = n_h l \sim 10^{19}$ cm^{-2} for the plasma density of the hot source $n_h \sim 2 \times 10^{10}$ cm^{-3} and the size of the loop-top hard X-ray source $l \sim 5 \times 10^3$ km. The corresponding stopping energy E [keV] of nonrelativistic electrons is estimated by

$$E = 1.1 \times 10^{-9} N^{0.5} \quad (8)$$

and is 3.4 keV (see, e.g., Jackson 1975, chap. 13). The column density required to stop $E = 50$ keV electrons is $N \sim 2 \times 10^{21}$ cm^{-2} , and the electrons have to bounce 200 times within the compact loop-top region for the thick target to be effective. Partial trapping may explain the loop-top hard X-ray source, and the actual requirement for the confinement may not be so stringent as obtained here. Nevertheless, we need an efficient mechanism to confine the nonthermal electrons in the small region of the loop-top hard X-rays. (Since the uncertainty in the estimated plasma density of the hot source is within a factor of 3 [§ 2.2], the

uncertainty in the number of bounce is 65–600. This uncertainty does not change the conclusion.)

3.2.2. Thermal Interpretation

Next, we assume that the loop-top hard X-ray source is of thermal origin (superhot source). The temperature and the emission measure of the superhot source are 133 MK and 10^{44} cm^{-3} , if we use the M1 (23–33 keV) and M2 (33–53 keV) channels of HXT to obtain the temperature (Masuda 1994). The temperature and the emission measure of the hot source obtained with SXT are 20 MK and 2×10^{48} cm^{-3} (emission measure per unit area $\sim 4 \times 10^{29}$ cm^{-5}). Although both the hot and superhot sources are essentially located at the same position in the impulsive phase, the total emission measure of the hot source is 2×10^4 times larger than that of the superhot source. Thus, the superhot source, even if it has extremely high temperature, is not seen in the SXT images, owing to its low emission measure as compared with that of the hot source and the flatness of the SXT filter response at high temperatures.

The mean free path of electrons in the superhot plasma is given by

$$l_{sh} \sim 9 \times 10^3 \frac{T_{sh}^2}{n_{sh}}, \quad (9)$$

where T_{sh} and n_{sh} are the temperature and the plasma density of the superhot plasma (see, e.g., Miyamoto 1989). The mean free path is $l_{sh} \sim 5 \times 10^{10}$ cm for $T_{sh} = 133$ MK and $n_{sh} = 3 \times 10^9$ cm^{-3} (to be derived in § 3.3). (The mean free path outside the superhot source is much smaller owing to higher plasma density.) Since the mean free path is far larger than the apparent size of the superhot source, we need a confinement mechanism of thermal electrons as in the nonthermal model. In this regard, there is no significant difference between the nonthermal and thermal models. From equation (8), the required column density N is $\sim 1.2 \times 10^{20}$ cm^{-2} for electrons with thermal energy (12 keV) and $\sim 2 \times 10^{21}$ cm^{-2} for 50 keV electrons.

3.2.3. Confinement of High-Energy Electrons

It is not possible to distinguish thermal (bulk energization) or nonthermal models for the loop-top hard X-ray source from the existing data set. There is, however, one common feature that needs to be addressed: in both models, electrons with energies of 30–50 keV responsible for the loop-top hard X-ray source have to be confined in the small region above the soft X-ray loop. We will argue in the subsequent sections that the loop-top hard X-ray source is located in between the two almost vertical slow shocks. This configuration may be able to confine the electrons with magnetic mirroring due to the slow shocks: the magnetic field strength of the upstream B_u is estimated to be 52 G, whereas the field strength of the downstream side (B_d), where the loop-top hard X-ray source is located, is only a few G as derived in § 2.5.

The pitch angle of the loss cone θ (angle with respect to the magnetic field direction) is given by

$$\sin^2 \theta = \frac{B_d}{B_u}, \quad (10)$$

and $\theta \sim 14^\circ$ for $B_u = 52$ G and $B_d = 3$ G. Since the region is highly collisionless for electrons responsible for the hard X-ray emission as we have seen, the electrons are mirrored in between the two slow shocks along the recon-

nected field lines that go through the shocks. Note that electrons may be confined only in the shock region. As the high-energy electrons propagate toward the soft X-ray loop, where the slow shocks may be weaker or may not exist, the loop-top hard X-ray source may no longer be confined. The hard X-ray source is vertically elongated at higher energies (Fig. 2), and the hard X-ray spectra appear to be harder with higher altitude (Masuda 1994). This feature may be consistent with above scenario.

In the subsequent sections, we assume that the hard X-ray source is of thermal origin, simply because the fast outflow can heat the plasma to such a high temperature with fast shock as we will see.

3.3. Physical Parameters of the Superhot Source

Since the apparent difference between the superhot and the hot components in source size is only a factor of 2–4, the size difference alone can not explain a 10^4 difference in emission measure. Here, we obtain the physical parameters of the superhot source. The superhot source is embedded in the hot source. Since the superhot source is seen for a few minutes, which is much longer than the dynamical timescale, pressure equilibrium must be established between the two sources:

$$n_{\text{sh}} T_{\text{sh}} = n_h T_h, \quad (11)$$

where n and T are plasma density and temperature, and the subscripts sh and h denote the superhot and hot sources. (Since plasma $\beta \gg 1$ in the downstream side of the slow shocks, we neglect the magnetic effect in the pressure balance of the two components.) The plasma density of the superhot source is then about $2 \times 10^{10} \text{ cm}^{-3} \times 20 \text{ MK}/133 \text{ MK} \sim 3 \times 10^9 \text{ cm}^{-3}$. (The filling factor of the hot component is assumed to be 1.0 in deriving the density n_h .) This density is much higher than the density ($3 \times 10^8 \text{ cm}^{-3}$) obtained from HXT observations (Masuda et al. 1995), because the filling factor of unity is assumed for the loop-top hard X-ray source in their analysis. The density of the superhot source is much lower than that of the hot source (Table 1). The escape of the fast electrons (§ 3.4) and the expansion of the superhot source due to dynamical pressure balance may result in a lower plasma density. The volume filling factor of the superhot source f is given by

$$f \equiv \frac{V_{\text{sh}}}{V_h} = \frac{\text{EM}_{\text{sh}}/n_{\text{sh}}^2}{\text{EM}_h/n_h^2}, \quad (12)$$

where V is the volume, and EM is the total emission measure. The filling factor of the superhot source is $f \sim 0.2\%$ of the hot component for parameters given in Table 1. The thermal energy content of the superhot source ($3kT_{\text{sh}} \text{EM}_{\text{sh}}/n_{\text{sh}} = 3p_{\text{sh}} \text{EM}_{\text{sh}}/2n_{\text{sh}}^2$) is only $f \sim 0.2\%$ of the hot component. We also estimate the dynamical timescale of the superhot source. The length scale of the superhot source is $l_{\text{sh}} \sim f^{1/3} l_h \sim 1157 \text{ km}$, where $l_h \sim 9 \times 10^3 \text{ km}$ is the scale size of the hot source. The dynamical timescale is then $l_{\text{sh}}/C_s \sim 0.6 \text{ s}$, where $C_s \sim 1914 \text{ km s}^{-1}$ is the sound speed of the superhot source with temperature of 133 MK.

3.4. Formation of Fast Shock

Although the overall spatial coincidence of the hot and superhot sources implies that the two temperature components are parts of the multitemperature (differential emission measure) structure of the plasmas commonly heated by the slow shocks, we suggest that this is not the case, simply

because the time evolution of the two components differs significantly. The loop-top hard X-ray source is seen only between 17:26 and 17:28 UT, whereas the temperature of the hot component stays almost constant throughout the observation. If the two components are heated commonly with the slow shocks, their time profiles should have coincided. If the hot source is maintained by the cooling of the superhot source, the time evolutions of the two components should have been more synchronous. We thus conclude that the superhot source is heated by a separate mechanism.

One possibility is fast bow shock (see, e.g., Landau & Lifshitz 1959, chap. 13) heating due to the collision of the supersonic downward outflow with the reconnected flux tube as inferred by Masuda et al. (1994) and Shibata et al. (1995a). We have shown in the previous section that the estimated outflow speed V_h exceeds the sound speed by a factor of 1.5–1.8. The condition for fast shock formation is $V_h^2 > C_s^2 + V_A^2 \sim C_s^2$, where C_s and V_A are the sound and Alfvén velocities of the downstream (Priest 1982, p. 189). Thus, the outflow speed satisfies the condition for the formation of a fast shock. If the magnetic field strength of the inflow is larger in the early phase of the flare, the sound Mach number of the outflow $M = V_h/C_s$ can be higher, and a stronger shock is expected. The Mach number gradually decreases with decreasing speed of the outflow jet, resulting in the fade-out of the shock, i.e., the fade-out of the loop-top hard X-ray source in the later phase of the flare. The extremely small emission measure of the superhot source suggests that the reconnection outflow is a highly collimated jet. The resulting superhot plasma thus occupies a small fraction of the hot source volume. The numerical simulations by Ugai (1987, 1996), Lee & Yan (1992), Forbes & Malherbe (1991), and Magara et al. (1996) predicted a situation close to the overall magnetic structure described here.

The temperature T_{sh} of the downstream side of the fast shock is given by

$$\frac{T_{\text{sh}}}{T_h} = \frac{[2\gamma M^2 - (\gamma - 1)][(\gamma + 1)M^2 + 2]}{(\gamma + 1)^2 M}, \quad (13)$$

where T_h is the temperature of the upstream side of the fast shock (hot source; downstream side of the slow shock), M is the Mach number of the upstream of the fast shock, and γ is the ratio of specific heats (see, e.g., Landau & Lifshitz 1959, chap. 9). $T_{\text{sh}} \sim 133 \text{ MK}$ and $T_h \sim 20 \text{ MK}$, and $T_{\text{sh}}/T_h \sim 6.5$. $M \sim 3.5$ is needed, if $\gamma = 1.1$ (quasi-isothermal case), and $M \sim 2.4$, if $\gamma = 5/3$ (adiabatic case). The required Mach number is slightly higher than the Mach number derived from the observations (1.5–1.8) even in the adiabatic case. This implies that the outflow jet has a higher speed with a small scale size, comparable to that of the superhot source. Lee & Yan (1992) showed from their numerical simulation that the outflow speed is spatially nonuniform in the downstream region: The speed is the highest just below the diffusion region and decreases closer to the slow shocks and the separatrix lines. This indicates that the high-speed jet needed for the strong fast-mode shock is available only below the diffusion region. This is consistent with the small scale size of the superhot source embedded in a larger hot source.

3.5. Energetics of Superhot Source

In this subsection, we discuss how the superhot source is energetically maintained. Note that the numbers given in

this and the next subsections are obtained from order-of-magnitude estimates. The primary energy-loss mechanism of the superhot source is conductive cooling. Since the mean free path is larger than the observed size of the superhot source, conductive loss is limited by the free-streaming of the superhot electrons. The energy loss in this regime is expressed as

$$E_{\text{sh}} \sim f^{2/3} s_h n_{\text{sh}} m_e v_{\text{th}}^3, \quad (14)$$

where f is the volume filling factor $\sim 2 \times 10^{-3}$ derived in § 3.1, s_h is the observed (cross-sectional) size of the hot source $\sim 9000 \text{ km} \times 9000 \text{ km}$, $n_{\text{sh}} \sim 3 \times 10^9 \text{ cm}^{-3}$ (Table 1), m_e is the electron rest mass, and v_{th} is the electron thermal velocity $\sim 6.3 \times 10^4 \text{ km s}^{-1}$ for $T_{\text{sh}} = 133 \text{ MK}$. The energy loss by free-streaming electrons is about $8.7 \times 10^{27} \text{ ergs s}^{-1}$ for these parameters. Since the thermal energy content of the superhot source is $3kT_{\text{sh}} EM_{\text{sh}}/n_{\text{sh}} \sim 1.9 \times 10^{27} \text{ ergs s}^{-1}$, the conductive cooling timescale is 0.2 s. Although the temperature of the superhot source is high, the heat flux (electron flux) is limited by the small filling factor of the superhot source, and by the free electron streaming situation. Since the heat flux may be further impeded by magnetic mirroring owing to the slow shocks and by the plasma microturbulence as well as the thermo-electric effect (Brown, Melrose, & Spicer 1979; Spicer 1977), this estimate is regarded as an upper limit. The estimated rate of the conduction loss from the superhot source ($8.7 \times 10^{27} \text{ ergs s}^{-1}$) agrees reasonably with the estimated outflow energy from the reconnection site ($2.4 \times 10^{27} \text{ ergs s}^{-1}$; see § 2.5). This means that the outflow energy is efficiently converted to plasma heating with the fast shock.

3.6. Superhot Source and Footpoint Hard X-Ray Sources

The total number of electrons in the superhot source is $EM_{\text{sh}}/n_{\text{sh}} \sim 3 \times 10^{34}$ electrons, and the number of electrons lost as free-streaming electrons is $f^{2/3} s_h n_{\text{sh}} v_{\text{th}} \sim 2.4 \times 10^{35} \text{ electrons s}^{-1}$. (This number should be regarded as an upper limit, since there must be some confinement mechanism such as the one discussed in § 3.2.3.) This means that all electrons are lost within 0.1 s, without a supply of electrons. The number of electrons supplied by the outflow is $s_d n_h V_h \sim 2 \times 10^{35} \text{ s}^{-1}$ for $s_d \sim 3000 \text{ km} \times 3000 \text{ km}$, $n_h \sim 2 \times 10^{10} \text{ cm}^{-3}$, and $V_h \sim 1144 \text{ km s}^{-1}$. Thus, the escaping electrons of the superhot source must be supplied from the outflow jet. These simple order-of-magnitude estimates indicate that the superhot source immediately disappears without continuous heating and a continuous supply of electrons from the outflow.

The significant flux of the escape electrons from the superhot source can contribute to the footpoint nonthermal emissions. The rate of escape of electrons from the superhot source ($2.4 \times 10^{35} \text{ electrons s}^{-1}$) is comparable to the number of electrons required for the thick-target footpoint emissions for this flare ($2 \times 10^{35} \text{ electrons s}^{-1}$; Table 3.2 of Masuda 1994). This implies the possibility that the escape electrons produce the footpoint hard X-ray sources. However, Figure 2 shows that the hard X-ray footpoint sources appear to be located inside the footpoints of the soft X-ray loop. Since the loop-top hard X-ray source is located above the soft X-ray loop, the connectivity between the loop-top source and the footpoint sources is not clear (Tsuneta 1995). Also, the escape electrons from the loop-top source with temperature of 100–150 MK alone can not

produce the “hard” hard X-ray spectra of impulsive flares in general. The role of the escape electrons for the footpoint thick-target emission is still an open question.

4. SUMMARY AND DISCUSSION

4.1. Impulsive and LDE Flares

The discovery of the hot source coincident in position with the hard X-ray source strongly suggests that magnetic reconnection occurs above the compact flare loop as in LDE flares. We have shown quantitatively that the hot source can be heated with the slow shocks. The only difference between the impulsive flare and LDE flares is the difference in the height of the X-point (diffusion region) where reconnection of magnetic fields takes place. If the X-point is located higher, the cusp structure will be naturally more significant, and the large-scale slow shock structure may be more clearly seen.

Observationally, the loop-top hard X-ray sources are less significant in LDE flares and are more often seen in impulsive flares. Whether the loop-top hard X-ray source is created or not critically depends on the Mach number of the outflow jet. The Mach number depends on the speed and the temperature of the outflow, both of which depend on the global conditions of the system. For instance, the higher X-point of LDE flares results in weaker magnetic fields in the inflow, which implies a lower outflow velocity. This may be the reason that most of LDE flares do not have significant loop-top hard X-ray sources. Conversely, if the cool channel with lower temperature develops, the loop-top hard X-ray source can be found in LDE-type flares: heating by the fast shocks may be more effective for flares or phases with lower loop-top temperatures, even if the outflow speed is the same.

We therefore argue that there is no essential difference in the mechanism of the flare energy release between compact-loop (impulsive) and long duration (LDE) flares. Note, however, that these arguments do not rule out other magnetic configurations of reconnection such as reconnection of emerging flux with existing coronal magnetic fields and/or reconnection of two or more independent magnetic loops.

4.2. Global Energetics of the Reconnection Region

We have speculated that high-energy electrons responsible for the impulsive loop-top hard X-ray emission are confined in between the slow shocks with magnetic mirroring. We have also assumed that the loop-top hard X-ray source is of thermal origin (superhot source). With this assumption, we have quantitatively understood the hot and superhot sources above the soft X-ray loop with slow and fast shock heating and have provided a consistent picture of the overall reconnection site. Here we summarize the global energetics of the loop-top region that emerges from the present analysis: The magnetic energy is converted to the plasma heating at the slow shock regions. The energy production rate is estimated to be $7.7 \times 10^{27} \text{ ergs s}^{-1}$. The heated plasma is seen as the 15–20 MK hot source above the reconnected flux tubes. Since the temperature of the hot source is almost constant, the slow shock heating continues throughout the flare.

In the early (impulsive) phase, a fast shock due to the collision of the supersonic outflow with the reconnected flux tubes can further heat the hot plasma and can produce the

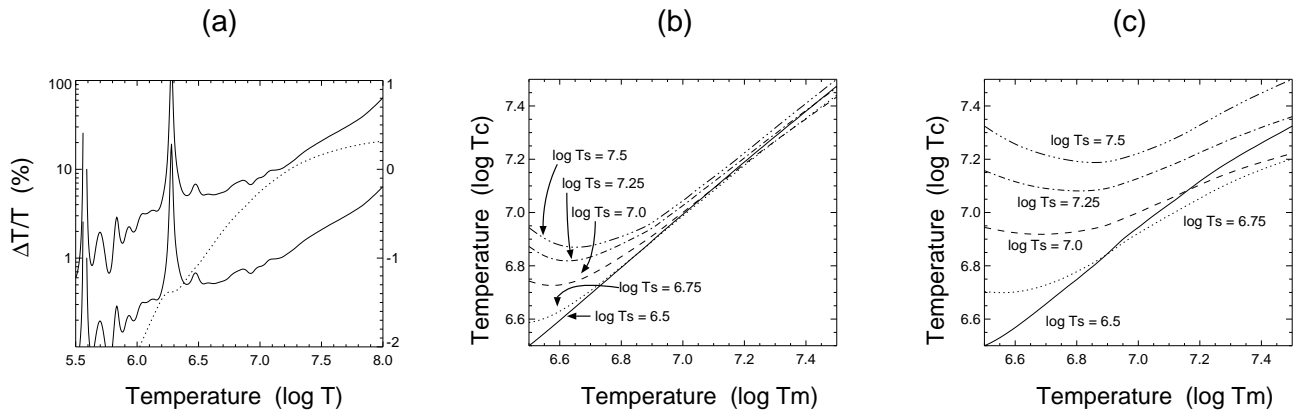


FIG. 7.—(a): Temperature error ΔT as a function of the true temperature T for 10% (thick line) and 1% (thin lines) errors in the ratio R of the two images (pixels) taken with thick aluminum and beryllium filters. The relation between the ratio R and the temperature T is also shown (dotted line). (b) and (c): Single temperature T_c is derived from the simulated filter ratio for plasmas with two temperature components; a main component with temperature T_m , and a subcomponent with temperature T_s . The derived temperature T_c is affected by the presence of the subcomponent T_s . (b) shows the case in which the emission measure of the subcomponent is 10% of the main component, and (c) is the case for 50%. The figures are taken from Yoshida (1996).

superhot source, if the Mach number of the outflow exceeds 1. The Mach number obtained from SXT observations (1.5–1.8) satisfies this condition, although a larger Mach number may be required to heat the 15 MK plasma to 133 MK with a fast shock. The outflow energy has to be efficiently converted to plasma heating to maintain the superhot hard X-ray source with a temperature exceeding 100 MK. The superhot source will disappear with a timescale shorter than the timescale of the flare if it is without a continuous supply of heating energy and fresh electrons. The extremely small emission measure of the hard X-ray source (as compared with that of the hot source) indicates that the superhot source has a spatial size smaller than apparent size of the hard X-ray source. This indicates a narrow outflow jet from the reconnection site with high Mach number.

The loop-top hard X-ray source is located in between the slow shocks and above the soft X-ray loop in this flare. Note, however, that according to the scenario presented in this paper, the loop-top hard X-ray sources are not necessarily located high above the soft X-ray loop. They can be closer to the soft X-ray loop: The location of the fast bow shock (i.e., the location of the loop-top hard X-ray source) depends on such parameters as the outflow speed (Mach number) and the speed of the chromospheric evaporation. It is important to derive the accurate locations of the loop-top hard X-ray sources observationally with respect to the soft X-ray loops in many flares.

4.3. Electron Acceleration and Fast Shock

The superhot source is seen only in the impulsive phase when the double footpoint hard X-ray sources are observed. Sakao et al. (1996b) and Sakao, Kosugi, & Makashima (1996a) showed that the footpoint hard X-ray emission is in general due to nonthermal electron beams. We speculate

from the time coincidence of the loop-top and footpoint hard X-ray emissions (Masuda et al. 1994) that the fast shock heating is causally related to the nonthermal acceleration of electrons. The condition for the formation of the fast shock (supersonic outflow) and/or the fast shock itself appear to be closely related to the nonthermal electron acceleration. The presence of the threshold for the formation of the fast shock makes the loop-top hard X-ray source more transient in nature. This may be related to the highly transient (high time variability) nature of the impulsive bursts. Although the estimated rate of escape electrons from the superhot source is close to the number of electrons required for the thick-target emission at the footpoints, additional acceleration processes may be required to explain the “hard” hard X-ray spectra.

The time-of-flight method (Aschwanden et al. 1996a, 1996b, 1996c) applied to this flare gave the conclusion that the site for the nonthermal electron acceleration is located in the small region above the loop-top hard X-ray source (stochastic electron acceleration, or acceleration by a super-Dreicer electric fields as applied to the short distance within the loop-top region) or that electrons are accelerated along the reconnected flux tubes (acceleration by sub-Dreicer DC electric field driven at the loop top and applied to the entire reconnected magnetic field lines that go through the loop-top region; Tsuneta 1995). Thus, the two independent observations (the present observation and the time-of-flight method) identify the loop-top region as an important region for driving particle acceleration.

S. T. would like to thank K. Shibata, T. Yoshida, M. Ugai, T. Yokoyama, and K. Hori for stimulating discussions. The authors also thank the anonymous referee for comments on the paper.

APPENDIX A

ESTIMATION OF TEMPERATURE ERROR

In this Appendix, we estimate three factors contributing to the error of the derived temperatures obtained with a pair of the broadband filters. The factors to be considered here are (1) incident photon noise, (2) scattering from the bright flare loop to dark regions, and (3) contribution of nonflaring line-of-sight corona.

A1. EFFECT OF POISSON NOISE

The accuracy of the derived temperatures depends on the incident photon statistics and the level of the scattering photons with respect to the level of the original signals. Figure 7a shows the temperature error ΔT , when the ratio of the intensity of the images taken with beryllium and thick aluminum filters have 1% or 10% errors (Yoshida 1996). The source of the error can be Poisson noise of incident photons and the scattering photons from the bright flare loops. The typical DN (data number, A/D converted intensity of a pixel) is $1\text{--}2 \times 10^4$ for the top of the bright flare loop and $1\text{--}4 \times 10^3$ for the hot source above the flare loop (after summation). The corresponding numbers of incident photons are 3000–6000 photons (flare loop) and 300–1300 photons (hot source). (3 DN approximately corresponds to one incident photon; Kano & Tsuneta 1995.) The filter ratio then has 3.6%–1.3% error (flare loop) and 5.8%–2.8% error (hot source). The resulting temperature error is within 2% (flare loop), and is within 5% (hot source) from Figure 7a. The 3×3 summation done before the temperature analysis improves the accuracy, and the actual error is smaller than these estimates. The Poisson noise error, however, increases with higher altitude above the hot source owing to the lower X-ray intensity.

A2. EFFECT OF SCATTERING

We estimate the effect of the scattered photons from the bright flare loop to the dark region. The scattering is due to the microroughness of the grazing incidence X-ray mirror and is represented by the power-law wing of the point-spread function. Hara et al. (1994) obtained the analytic form of the wing component for the thin aluminum filter, using the in-flight flare data. We estimate the number of the scattered photons from bright soft X-ray loop with the wing component of the point-spread function given by Hara et al. (1994).

We define the scattering ratio (in each pixel), which is the ratio of the observed X-ray signal with the scattering signal to that pixel from all over the field of view of the partial frame image. Most of the scattered photons come from the bright flare loop. The scattering ratio reaches 40% inside the limb, where the observed signals are fainter than that above the limb. The scattering signals are below 15% in the bright flare loop and the hot source above the flare loop. The west end of the frames also has a lower scattering contribution because of the expanding loops reported by Shibata et al. (1995a). The expanding looplike structure is slightly brighter than the surrounding corona, which results in an apparent decrease in the scattering ratio. The region in between the flare loop and the expanding loop structure has higher scattering contribution reaching 20%–40%.

Scattering affects both the thick aluminum and beryllium images more or less in the same way. If we assume that the filter ratio R has the same amount of the error as the scattering ratio, only the flare loop and the hot source have temperature errors below 10%. The temperatures of the region above the hot source may have a higher error in temperature. We did not obtain the temperatures inside the limb because of the higher scattering contamination.

A3. EFFECT OF LINE-OF-SIGHT CORONA

The X-ray intensity above the bright soft X-ray loop decreases with increasing height. This means that X-rays from the line-of-sight nonflaring corona potentially contribute more in these dim regions, if the emission measure of the line-of-sight active region is not negligible as compared with that of the flare plasma. Figures 7b and 7c show how the temperature T_c derived with two broadband filters (under the assumption of isothermality) is affected by the addition of the component with temperature T_s to the main component with temperature T_m (Yoshida 1996). (If there is no subcomponent T_s , the derived temperature T_c should match the true temperature T_m .) The main component corresponds to the flare-related plasmas, and the subcomponent corresponds to the nonflaring line-of-sight corona. A single temperature T_c is derived from the simulated filter ratio for plasmas consisting of these two temperature components T_m and T_s .

Figure 7b shows the case that the emission measure of the subcomponent is 10% of the main component, and Figure 7c is the case for 50%. If the contamination of the subcomponent is 10%, the derived temperature T_c will not be affected by the subcomponent with any temperature T_s . If the contamination of the subcomponent is 50%, the true temperature T_m of 20 MK is, for instance, affected by the active region corona with temperature T_s of 3–5 MK, and the derived temperature T_c is 12–15 MK (about 5–8 MK lower than the temperature of the main component). The line-of-sight emission measure that affects the temperature analysis is mostly that of the active region with temperature 4–5 MK. The emission measure of the quiet Sun is too low in temperature (2 MK) to affect the temperature analysis of the flare plasma.

The observed emission measure above the hot source (and below the expanding loop structure) is about 2 times higher than that at the northwest corner (Fig. 3), which may be dominated by the active region corona. Thus, the emission-measure contribution from the active region corona may reach 50% above the hot source. Figures 3 and 6 show gradual decrease in temperature above the hot source with height. It is, however, not clear that this (the decrease of the temperature with height) is the real structure or is due to the increasing contamination of the line-of-sight active region corona with height. In the latter case, even if the temperature is the same or even increases with height, the derived temperatures obtained with the broadband filters will decrease.

REFERENCES

- Aschwanden, M. J., Hudson, H. S., Kosugi, T., & Schwartz, R. A. 1996a, *ApJ*, 464, 985
 Aschwanden, M. J., Kosugi, T., Hudson, H. S., Wills, M. J., & Schwartz, R. A. 1996b, *ApJ*, 470, 1198
 Aschwanden, M. J., Wills, M. J., Hudson, H. S., Kosugi, T., & Schwartz, R. A. 1996c, *ApJ*, 468, 398
 Brown, J. C. 1971, *Sol. Phys.*, 18, 489
 Brown, J. C., Melrose, D. B., & Spicer, D. S. 1979, *ApJ*, 228, 592
 Cargill P. J., & Priest, E. R. 1983, *ApJ*, 266, 383
 Carmichael, H. 1964, in AAS–NASA Symposium on Solar Flares, ed. W. N. Hess (NASA SP-50), 451
 Forbes, T. G., & Acton, L. W. 1996, *ApJ*, 459, 330
 Forbes, T. G., & Malherbe, J. M. 1991, *Sol. Phys.*, 135, 361
 Hara, H., Tsuneta, S., Acton, L. W., Bruner, M. E., Lemen, J. R., & Ogawara, Y. 1994, *PASJ*, 46, 493
 Hirayama, T. 1974, *Sol. Phys.*, 34, 323

- Jackson, J. D. 1975, *Classical Electrodynamics* (New York: John Wiley & Sons)
- Kano, R., & Tsuneta, S. 1995, *ApJ*, 454, 934
- Kopp, R. A., & Pneuman, G. W. 1976, *Sol. Phys.*, 50, 85
- Landau, L. D., & Lifshitz, E. M. 1959, *Fluid Mechanics* (London: Pergamon)
- Lee, L. C., & Yan, M. 1992, *Phys. Fluids B*, 4(11), 3808
- MacCombie, W. J., & Rust, D. M. 1979, *Sol. Phys.*, 61, 69
- Magara, T., Mineshige, S., Yokoyama, T., & Shibata, K. 1996, *ApJ*, 466, 1054
- Masuda, S. 1994, Ph.D. thesis, Univ. Tokyo
- Masuda, S., Kosugi, T., Hara, H., Sakao, T., Shibata, K., & Tsuneta, S. 1995, *PASJ*, 47, 677
- Masuda, S., Kosugi, T., Hara, H., Tsuneta, S., & Ogawara, Y. 1994, *Nature*, 371, 495
- Miyamoto, K. 1989, *Plasma Physics for Nuclear Fusion* (Cambridge: MIT Press)
- Ogawara, Y., Takano, T., Kato, T., Kosugi, T., Tsuneta, S., Watanabe, T., Kondo, I., & Uchida, Y. 1991, *Sol. Phys.*, 136, 1
- Petschek, H. E. 1964, in *AAS-NASA Symp. on Solar Flares*, ed. W. N. Hess (NASA SP-50), 425
- Priest, E. R. 1982, *Solar Magnetohydrodynamics* (Dordrecht: Reidel)
- Priest, E. R., & Forbes, T. G. 1986, *J. Geophys. Res.*, 91, 5579
- Sakao, T., Kosugi, K., & Makishima, K. 1996a, *PASJ*, in press
- Sakao, T., Kosugi, K., Masuda, S., Makishima, K., Ina-Koide, M., & Murakami, T. 1996b, *PASJ*, in press
- Shibata, K., Masuda, S., Shimojo, M., Hara, H., Yokoyama, T., Tsuneta, S., Kosugi, T., & Ogawara, Y. 1995a, *ApJ*, 451, L83
- Shibata, K., Yokoyama, T., & Shimojo, M. 1995b, *Adv. Space Res.*, 17(4/5), 197
- Shimizu, T., Tsuneta, S., Acton, L. W., Lemen, J. R., Ogawara, Y., & Uchida, Y. 1994, *ApJ*, 422, 906
- Shimizu, T., Tsuneta, S., Acton, L. W., Lemen, J. R., & Uchida, Y. 1992, *PASJ*, 44, L147
- Shimojo, M., Hashimoto, S., Shibata, K., Hirayama, T., Hudson, H. S., & Acton, L. W. 1996, *PASJ*, 48, 123
- Spicer, D. S. 1977, *Sol. Phys.*, 54, 379
- Sturrock, P. A. 1966, *Nature*, 211, 695
- , ed. 1980, *Solar Flares: A Monograph from Skylab Solar Workshop II* (Boulder: Colorado Associated University Press)
- Tsuneta, S. 1993, in *IAU Colloq. 141, The Magnetic and Velocity Fields of Solar Active Regions*, ed. H. Zirin, G. Ai, & H. Wang (ASP Conf. Proc. 46) (San Francisco: ASP), 239
- . 1995, *PASJ*, 47, 691
- . 1996a, *ApJ*, 456, 840
- . 1996b, in *IAU Colloq. 153, Magnetodynamic Phenomena in the Solar Atmosphere*, ed. Y. Uchida et al. (Dordrecht: Kluwer), 161
- Tsuneta, S., Hara, H., Shimizu, T., Acton, L. W., Strong, K. T., Hudson, H. S., & Ogawara, Y. 1992, *PASJ*, 44, L63
- Ugai, M. 1987, *Geophys. Res. Lett.*, 14, 103
- . 1996, *Phys. Plasmas*, 3, 4172
- Yokoyama, T. 1995, Ph. D. thesis, National Astronomical Observatory, Tokyo
- Yokoyama, T., & Shibata, K. 1996, *PASJ*, 48, 353
- Yoshida, T. 1996, Master's thesis, Univ. Tokyo
- Yoshida, T., & Tsuneta, S. 1996, *ApJ*, 459, 342